Published in final edited form as:

Neuroimage. 2021 January 01; 224: 117355. doi:10.1016/j.neuroimage.2020.117355.

A 3-axis coil design for multichannel TMS arrays

Lucia I. Navarro de Lara[a,*], **Mohammad Daneshzand**[a], **Anthony Mascarenas**[b], **Douglas Paulson**[b], **Kevin Pratt**[b], **Yoshio Okada**[d], **Tommi Raij**[e,f], **Sergey N. Makarov**[a,c], **Aapo Nummenmaa**[a,*]

[a]Athinoula A. Martinos Center for Biomedical Imaging, Department of Radiology, Harvard Medical School, Massachusetts General Hospital, Charlestown, MA 02129, USA

[b]Tristan Technologies, San Diego, CA 92121, USA

[c]Department of Electrical and Computer Engineering, Worcester Polytechnic Institute, Worcester, MA 01609, USA

[d]Moment Technologies LLC, Charlestown, MA, USA

[e]Center for Brain Stimulation, Shirley Ryan AbilityLab, Chicago IL 60611 USA

[f]Department of Physical Medicine and Rehabilitation, Department of Neurobiology, Northwestern University, Chicago IL 60611 USA

Abstract

Purpose: Multichannel Transcranial Magnetic Stimulation (mTMS) arrays enable multiple sites to be stimulated simultaneously or sequentially under electronic control without moving the system's stimulation coils. Here, we build and characterize the performance of a novel modular 3-axis TMS coil that can be utilized as a unit element in large-scale multichannel TMS arrays.

Methods: We determined the basic physical characteristics of the 3-axis TMS coil *x*-, *y*- and *z*-elements using a custom 2-channel programmable stimulator prototype. We mapped the temporal rate-of-change of the induced magnetic field (*dB/dt*) on a 2D plane parallel to the coil surface (including an extended line for full spatial coverage) and compared those values with predictions from magnetic field simulations. Temperature measurements were carried out to assess the incorporated air-cooling method. We measured the mutual and self-inductances of the *x/y/z*-elements to assess coupling between them. Additionally, we measured and calculated the coupling

*Corresponding authors. lnavarrodelara@mgh.harvard.edu (L.I. Navarro de Lara), anummenmaa@mgh.harvard.edu (A. Nummenmaa).

Author contribution statement

L.N.L. collected all experimental data of the 3-axis TMS coil, performed simulations of the 3-axis TMS dB/dt fields, and had the principal responsibility of manuscript writing.

M.D. performed all computational E-field analyses for the commercial TMS coils, 3-axis TMS coil as well as the multichannel targeting, and contributed to manuscript writing.

A.M., D.P., K.P. contributed to the original design and fabricated the 3-axis TMS prototype.

Y.O. and T.R. contributed to the conception of the research idea and participated in manuscript writing.

S.N.M. contributed to the computational E-field analysis including high-resolution modeling of the 3-axis TMS coil and wrote the numerical routines for the inductance estimation.

A.N. conceived the original research idea, supervised all empirical and computational analyses, and participated in manuscript writing.

Supplementary materials

Supplementary material associated with this article can be found, in the online version, at doi: 10.1016/j.neuroimage.2020.117355.

between *z*-elements in the array configuration. Finally, we performed electric field simulations to evaluate the stimulation intensity and focality of the coil and compared the results to conventional TMS coils as well as demonstrated suitability of the 3-axis coil for a multichannel array configuration.

Results: The experimentally obtained *dB/dt* values validated the computational model of the 3-axis coil and therefore confirmed that both the coil and stimulator system are operating as intended. The air-cooling system was effective for brief high-frequency pulse trains and extended single- and paired-pulse TMS protocols. The electromagnetic simulations suggested that an array of the 3-axis coils would have comparable stimulation intensity to conventional TMS coils, therefore enabling clearly suprathreshold stimulation of the human brain. The recorded coil coupling between the *x/y/z*-elements was $< 1\%$ and the maximal coupling between *z*-elements in the array configuration was 1.8% and 3.4% for the measured and calculated values, respectively.

Conclusion: We presented a 3-axis coil intended for multichannel TMS arrays. The electromagnetic measurements and simulations verified that the coil fabrication met the desired specifications and that the inductive coupling between the elements was negligible. The air-cooled 3-axis TMS coil appears suitable to be used as an element in multichannel TMS arrays.

Keywords

Multichannel TMS; 3-axis coil; E-field simulations; TMS array

1. Introduction

Transcranial magnetic stimulation (TMS) enables safe and efficient stimulation of the human brain noninvasively (Barker et al., 1985). It is currently the only non-invasive tool to induce clearly suprathreshold stimulation resulting in action potentials in cortical neurons in a painless way. Therefore, it has become one of the most widely used neuromodulation technologies for both basic science and the clinic. To date, most applications are based on single-channel TMS used in conjunction with neuronavigation systems that enable accurate and reproducible targeting of superficial brain areas (Ruohonen and Karhu, 2010). The single-channel TMS technique has been extended to enable bi-focal settings by using two independent coils and stimulators (Ferbert et al., 1992). Furthermore, specific coils have been designed in order to probe the connectivity between two nearby nodes in cortical networks yielding new data on their functional relationships (Groppa et al., 2012). Another study has demonstrated up to four-channel systems to enable more flexible spatiotemporal control of the stimuli (Roth et al., 2014). However, it is clear that large-scale multichannel TMS systems are needed to fully generalize this technique to study the causal relationships and the propagation of activity between different areas participating in distributed cortical processing.

Multichannel TMS arrays have been proposed to enable focusing of the induced electric field (E-field) without any physical movement of the coils (Ruohonen and Ilmoniemi, 1998) where focusing is achieved by combining individual TMS coils of the array with current amplitudes weighted such that the resultant field will generate a ‘hot spot’ to a desired target location. The unique feature of such a large-scale TMS array system is that the location of

the ‘hot spot’ can be moved rapidly under electronic control and therefore different targets can be activated with millisecond-level temporal accuracy. While robotic TMS coil positioning (Lancaster et al., 2004) provides arguably the most accurate targeting (Goetz et al., 2019), moving the coil from one target to another will be inherently sluggish due to the obvious safety concerns associated with automated rapid physical coil movement. While the TMS array concept is simple, construction of the first set of large-scale systems has necessitated tackling several technological challenges.

The first major challenge faced by TMS array systems is the development of stimulator systems that are capable of accurately controlling the timing of discharging multiple stimulator units as well as being scalable for a large number of channels with a feasible cost and physical footprint. Here, we demonstrate the use of a dedicated two-channel prototype manufactured by MagVenture (Farum, Denmark) that is based on modular design readily extendable with additional channels. The individual channels in our system adopt the basic biphasic stimulator circuit, whereas other groups have also successfully demonstrated 2-channel systems utilizing a H-bridge type design for the stimulator (Koponen et al., 2018). The second major challenge is ensuring accurate and efficient stimulation of cortical targets based on the design of the basic coil elements as well as their array configuration. The most straightforward array configuration that was originally proposed (Ruohonen and Ilmoniemi, 1998), consisting of circular coil elements placed on rectangular or hexagonal lattice, faces certain challenges in this domain. The main issue is that a circular coil produces zero E-field field in its center, leading to that neighboring coils must be used to stimulate this location, which results in reduced stimulation intensity, especially for arrays with larger diameter coil elements with increased distance between the coil centers. Adding a second ‘layer’ of coils with center positions shifted by half of the lattice spacing have been proposed to mitigate this issue (Han et al., 2004), but in this case the coupling between the coils becomes an issue. More recently, an approach in which multiple coils are vertically stacked with orthogonalized winding patterns has been proposed, and this appears to be a technically viable solution as demonstrated by a recent two-channel application (Koponen et al., 2018). However, the placement of several extended TMS transducer elements in an array configuration over the head such that the gaps between the wire windings and scalp is minimized everywhere may be challenging.

In this article, we design, build and validate a 3-axis coil as the element for general-purpose multichannel TMS array systems. The 3-axis coil, a compact multichannel TMS assembly, comprises of a circular *z*-element oriented parallel to the scalp surface combined with an *x/y*-element that is wound on a spherical coil form with interlaced windings. Our design is motivated by several key factors that contribute to the overall performance and feasibility of employing these types of TMS units in a multichannel array. First, the *x/y*-element will mitigate the issue of stimulating the cortical locations at which the *z*-element produces zero field as well as add degrees of freedom to the overall field shaping capabilities of the array. Second, all *x/y/z*-elements are geometrically inductively decoupled ensuring that the principle of superposition applies for the computational coil combination for multichannel targeting. Third, the use of relatively small diameter units enables conformal positioning of the coil unit with respect to the subjects’ head to maximize stimulation accuracy and intensity. Fourth, the coil elements can be cooled by air, cost-effectively fabricated, and after

their lifetime has been exceeded, they can be easily replaced. Fifth, the systems can be implemented in a fully modular fashion by adding as many 3-axis units as desired and the elements can be easily re-configured to optimize the performance for a given experiment. Finally, the overarching goal of our 3-axis coil system development is compatibility with a 3T MRI instrumentation and scanner environment (Navarro de Lara et al., 2020), which has further motivated us to employ modular TMS coil units with a relatively small outer diameter (~5 cm).

The article is organized such that first we present the concept of the 3-axis coil and describe its design and fabrication. Then we present the methods used to map the magnetic fields and how this information is used to validate the computational electromagnetic model of the coil. Next, we use computational modeling to quantify the electric field (E-field) profiles of the *x/y/z*-elements and their characteristics and to compare the results to commercially available coils in terms of the stimulation intensity and spatial focality. We then address the topic of heating of the coil assembly and demonstrate that our relatively simple air-cooling strategy enables trains of repetitive TMS (rTMS) and other temporally extended stimulation sequences. We quantify the coupling between the *x/y/z*-elements in a unit and the coupling between *z*-elements in an array configuration and show that the geometric decoupling of the elements is robust, resulting in the principle of superposition holding for simultaneous activation of multiple elements. To illustrate the capability to precisely control the timing of the stimulation pulses we show the capability to 'rotate' the induced field with timesteps of 100 ms. We conclude by demonstrating how these coils can be utilized to efficiently stimulate different cortical targets without any coil movement in a multichannel TMS array configuration using the computational targeting approach.

2. Material and methods

2.1. 3-axis coil concept, design and fabrication

The basic concept of the 3-axis coil design is shown in Fig. 1A. It consists of three orthogonal separate solenoid elements, where *x*-and *y*-elements are wound on a spherically symmetric coil form in an interlaced fashion (the coil dimensions are as annotated in the figure). The outer layer of the *x*-element has 10 turns and the inner layer 8 turns whereas the outer layer of the *y*-element consists of 12 turns and the inner 10 turns. The reason for the difference in the number of turns is to match the final inductance of both coils, given the difference in the radii of the spherical surfaces that accommodate the *x/y* windings. The *z*-element wire winding pattern is designed to allow positioning of the *x/y*-elements as close to the bottom of the entire 3-axis assembly as possible. The *z*-element has six turns at the bottom layer and five, four, and three turns on the next three layers, respectively. All three elements were designed to have similar inductance to produce matched stimulation pulse width when connected to standard bi-phasic TMS stimulators.

Fabrication of the 3-axis coil prototype was performed by Tristan Technologies (San Diego, CA, USA). Different steps of the design and fabrication process are shown in Fig. 1B–D. The coils were wound using Litz wire with an outer diameter of 2 mm (New England Wires, Lisbon, NH, USA). Air-cooling was incorporated to the coil design to increase the number of pulses that can be delivered without exceeding the safety limits for temperature. The air is

injected through the center of the coil allowing efficient circulation around the *x/y*-elements and guided through the opening in the *z*-element to reach the bottom of the coil assembly and finally removed through a side outlet (see Fig. 1B). For continuous monitoring of the temperature on each individual coil, an integrated circuit temperature transducer (AD592, Analog Devices, Norwood, MA, USA) is permanently attached to each individual element (see Fig. 1C). A photograph of the final prototype is shown in Fig. 1D. The housing of the coil was made of glass filled nylon.

2.2. Two-channel programmable MagVenture TMS stimulator system

The 3-axis coil was tested using a two-channel stimulator (Fig. 1E) that was custom-built by MagVenture (Farum, Denmark). This system serves as a prototype of a full-scale 16-channel stimulator system that is currently being assembled and installed at MGH Martinos Center. The fully programmable prototype is capable of producing bi-phasic pulses including repetitive stimulation, but the charging voltage is limited to 900 V (half of MagVenture MagPro X100). The timing and intensity of the pulses is configured using an executable pulse protocol offering microsecond temporal resolution, which is useful in setting precise delays between the channels/elements.

2.3. Magnetic field mapping for the 3-axis coil

To test the performance of the 3-axis coil and to validate the computational electromagnetic modelling results, we performed comprehensive magnetic field (B-field) mapping. The mapping was carried out by utilizing a commercially available calibrated three-axis probe: the MagProbe 3D (MagVenture, Farum, Denmark). This tool was used to measure the temporal rate-of-change (*dB/dt*) of the magnetic field at multiple spatial locations. The output of the probe is a voltage signal related to the *dB/dt* for each of the three Cartesian (*x*, *y* and *z*) field components with a conversion factor of 1 V per 1.4 kT/s. The measurement setup is shown in Fig. 3A. Data were collected on a 4 cm^2 plane using a 5 × 5 grid at 3.3 cm under the *z*-element windings (Fig. 3A). The 3.3 cm distance corresponds to the sum of the grid disk thickness (2.5 cm), the thickness of the double-sided tape used to attach the disk to the *z*-element (0.2 cm), the radius of the MagProbe 3D pickup loops (0.5 cm) and finally 0.1 cm left between the probe and the disk to move the probe freely using a micromanipulator (see bottom of Fig. 3A). We mounted a 2.5 cm disk under the coil to (i) evaluate the coil performance at the typical target depth for human TMS which is between 2 and 3 cm and (ii) to facilitate spatial sampling of the signals for the comparison with the simulated fields. Additionally, we acquired data along the x-axis in 0.5 cm steps from −8 cm to +8 cm to obtain spatially more extended one-dimensional line profiles of the fields. The three output connectors of the MagProbe 3D were directly connected to a data acquisition (DAQ) device (NI USB-6356, National Instruments, Austin, TX, USA). The DAQ device was connected *via* USB to a laptop running an in-house written script to collect the data employing the MATLAB data-acquisition toolbox (Mathworks, Natick, MA, USA). For each measurement point for the field mapping, five stimulation pulses at 50% maximal stimulator output (MSO) were delivered each second in a 10 s acquisition frame. The sampling frequency of the DAQ was set to 500 Ksamples/s.

We utilized MATLAB also for all data post-processing and analysis tasks. We used the initial (maximal) peak values of each acquired pulse on the probe outputs to define the intensity and the polarity of the produced *dB/dt* waveform. All five peak values were subsequently identified in the data time series of each spatial component and averaged to produce the final estimates. Below, we report these estimates in the analyses and figures pertaining to *dB/dt* values.

The maximal current rate-of-change *dI/dt* delivered by the stimulator is a value measured internally and reported by commercial MagPro X100 stimulators and is required for the electromagnetic field modeling of the coil (similarly to *dB/dt* the maximum occurs at the beginning of each pulse). The circuitry to measure and output the realized *dI/dt* was not implemented for the 2-channel programmable stimulator prototype. To obtain an estimate of the delivered maximal current rate *dI/dt* by the 2-channel programmable stimulator prototype each of the *x/y/z*-elements was separately connected and subsequently discharged using the MagPro X100 stimulator (MagVenture, Farum, Denmark). The stimulator output intensity was increased in 10% steps from 10% to 100% MSO intensity corresponding to 1800 V. The reported *dI/dt* values were recorded together with the measured peaks of the *dB/dt* components on the origin of the grid shown in Fig. 3A. Finally, each of the *x/y/z*-elements were discharged with the 2-channel programmable stimulator prototype at 50% to record the *dB/dt* values and the empirical *dI/dt* were extrapolated using the calibration measurement done with the MagPro X100.

2.4. Electromagnetic field modeling of the 3-axis coil and multichannel targeting

To compare the measured values against predictions from electromagnetic modeling, the *dB/dt* was evaluated at 3.3 cm from the coil bottom separately for each element. Modeling results were computed using custom MATLAB tools based on the Boundary Element Method accelerated with Fast Multipole Method (BEM-FMM) as detailed in (Makarov et al., 2018). Even though analytical expression exists, we used the FMM acceleration to evaluate the magnetic fields from the high-resolution discretized coil models to maintain numerical consistency across the results. The *dI/dt* values used in the simulations were obtained from the measured data as described in 2.3.

We also utilized the BEM-FMM approach to estimate and visualize the induced electric fields (E-fields) for various cases (Fig. 4A, Fig. 5A, and Fig. S3). For these simulations we extrapolated the *dI/dt* values for the *x*-, *y*- and *z*-elements from the values listed in Fig. 2C. Either a spherically symmetric head model or an anatomically realistic head model was used. The meshes corresponding to different tissue compartments for the anatomically realistic head model were obtained from Human Connectome Project (HCP) datasets (Van Essen et al., 2012) using the SimNIBS software (Windhoff et al., 2013) version 2.1 with an average mesh edge length of 1 mm as described in detail in (Htet et al., 2019a). For a high-resolution head model with ~1 million facets the algorithm took 200 s (10 s per iteration). The tissue conductivities for skin, skull, CSF, white and gray matter were 0.3, 0.02, 2.0, 0.106, and 0.065, respectively. With 20 iterations of the Generalized Minimal Residual Method (GMRS), the solution converged to a residual less than 0.00001. As pre-existing

freely available MRI data were used for all the simulations, no IRB-approved human subject study protocol was required.

Finally, to demonstrate the suitability of the 3-axis coil to be used in multichannel TMS arrays, we implemented computational targeting by placing 16 3-axis coils at approximately equal distances from the surface of the head (Fig. 9A). The resulting array comprises of forty-eight (16×3) independent elements that can be activated to achieve stimulation of a desired target. We applied the minimum norm estimate (MNE) method (Ruohonen and Ilmoniemi, 1998) to determine the required current rates (*dI/dt*) for all forty-eight elements to precisely stimulate a target location with a defined field intensity and orientation. To demonstrate that the 3-axis multichannel array should be able to readily reach suprathreshold intensities we explicitly limit the *dI/dt* values to 50% MSO in a subsequent constrained optimization step. All computations were done in MATLAB 2019a on a Xeon E5–2690 2.60 GHz PC with 128GB of RAM.

2.5. Temperature measurements for characterizing the air-cooling performance

The temperature timecourses of the *x*-, *y*-, and *z*-elements were measured using the incorporated sensors for 6 min after delivering one train of 20 pulses during 1 s at 75% of MSO of the MagPro X100 (MagVenture, Farum, Denmark) activating one element at a time. The measurements were done both without any cooling as well as with air that was cooled to 12° – 15 °C by letting the air flow through a metal tube immersed in an ice water bath. We used a constant flow of 3 standard cubic feet per minute (scfm) to perform the tests under conservative conditions. To convert the current delivered by the sensors (1 μA/°K) to a voltage, 1 K Ω through hole resistors 5% tolerance (Yageo, New Taipei City, Taiwan) were used. Neither amplification of the signal nor calibration was implemented. The voltages across the resistances were measured by the NI DAQ device connected *via* USB to a laptop running a custom MATLAB script to acquire the data with a sample rate of 20 kSamples/s. The set-up is shown in Fig. 6A.

The acquired data were processed with a median filter of order 100, converted to °C and plotted in MATLAB as difference to baseline temperature (Δ°C). From the filtered signal, the maximal temperature change per pulse was calculated using custom MATLAB scripts. The cooling curves, defined here as the portion of the data after the temperature maximum is reached, were fitted with exponential functions using the MATLAB “Curve Fitting Toolbox”. The goodness of the fit (R^2) was reported for each curve. The half time for each curve was calculated from the obtained exponential coefficients.

2.6. *Assessing the coupling between the x/y/z-elements in a TMS unit and the coupling between z-elements of different units in the array configuration*

First, we measured the inductances L_x, L_y and L_z of all three elements of the 3-axis TMS prototype and the mutual inductances M_{xy}, M_{xz} and M_{yz} between them in a single unit. To estimate the coupling between the *z*-elements in the array configuration, we constructed an additional coil consisting of a single *z*-element with the same dimensions as the *z*-element of the 3-axis TMS coil prototype. Subsequently, we measured M_{zz} between the *z*-elements of the 3-axis TMS coil prototype and the additional single coil in the array configuration. The

measurements were done using the Bench LCR/ESR Meter (Model 889, BK Precision, Yorba Linda, CA, USA) at a frequency of 10 kHz. The resistance for each element of the 3-axis TMS coil was also measured with this multimeter. For the array configuration, we measured the mutual inductance between the *z*-elements for the positions in the left hemisphere (TMS units 1 to 9, see Fig. S1 for the 3-axis TMS array layout). Additionally, we measured the mutual inductance between the *z*-elements for the positions 4 and 10. We assumed that the *z*-element intercoupling between hemispheres will be less than 0.5%, and for the right hemisphere the values should be similar due to the symmetry of the layout. For the mutual inductances, the $L_{inphase}$ and the $L_{revphase}$ were measured for each combination and the mutual inductance and coupling factor were calculated as follows:

$$\begin{aligned} L_{inphase} = L_1 + L_2 + 2M_{12},\ L_{revphase} = L_1 + L_2 - 2M_{12} \\ M_{12} = \left(L_{inphase} - L_{revphase}\right)/4 \end{aligned} \tag{1}$$

$$\mu_{12} = \frac{M_{12}}{\sqrt{L_1 \cdot L_2}} \tag{2}$$

Finally, we performed computational estimation of the mutual inductance between all *x/y/z*-elements in the array configuration. The mutual and self-inductances were calculated by discretizing the coil model meshes and calculating the Neumann integrals. The Neumann integral was evaluated for 256 discretized points on the coil model with a uniform current distributions across the wire using the FMM method (Makarov et al., 2018) for computational speed up. The FMM allows rapid evaluation of the Laplace potential-like terms between the current elements that are used to determine the numerical solution of Neumann integrals for the mutual and self-inductances of the coils. The method was validated with standard analytical expressions available for circular current loops.

In order to further characterize the potential coupling between the *x*-, *y*- and *z*-elements, the two-channel programmable stimulator prototype was used to pulse two elements either sequentially or simultaneously. The measurement of the induced fields was done as described in 2.3. The acquired *dB/dt* values for simultaneous discharge were compared to the computational summation of the field measurements of each individual element to investigate if linear superposition holds. The percentage average of the normalized difference between the results was calculated as:

$$\rho_{xy} = \text{mean}\left(\frac{dB/dt_{x\&y} - \left(dB/dt_x + dB/dt_y\right)}{dB/dt_x + dB/dt_y}\right) \cdot 100\% \tag{3}$$

where $dB/dt_{x\&y}$ are the results obtained when *x*- and *y*-elements were fired simultaneously and $dB/dt_x + dB/dt_y$ is the summation of the *x*- and *y*-element single measurement results. This quantity was also reported for the other two possible combinations, ρ_{xz} and ρ_{yz}.

3. Results

3.1. Three-axis TMS coil magnetic pulse measurements

First, we compared the magnetic pulses from the 2-channel programmable stimulator prototype to those of the MagPro X100. Fig. 2A illustrates the measured waveforms for the intensities ranging from 10% to 50% of the MSO of the MagPro X100 *vs.* the 2-channel stimulator for the *y*-element. The measurements verify that the custom-made 2-channel system and the MagPro X100 produce highly similar current pulses in the coils. The time courses of the stimulation pulses measured at the origin of the measurement grid (Fig. 3A) for each *x/y/z*-element are depicted in Fig. 2B. The obtained pulse widths for the *x, y,* and *z*-elements were 318 μs, 326 μs, and 330 μs, respectively.

After confirming the that the pulse waveforms and amplitudes are highly similar in the range of 0 – 900 V for both stimulators we obtained the experimental maximal *dI/dt* values as described in 2.3. using the data from MagPro X100. The results are summarized in Fig. 2C (only values from 10% to 50% are shown). Based on these values we extrapolated that the maximal *dI/dt* for each element of the 3-axis coil at 50% MSO using the 2-channel programmable stimulator prototype were 64.6 A/μs, 64.7 A/μs, and 58.4 A/μs for the *x, y,* and *z*-elements, respectively.

3.2. *Measured* vs. *simulated field maps*

Fig. 3B shows the magnetic field data for each coil component and for each cartesian component on a 2D plane using different scales to facilitate visualization. As expected, the *z*-element produces largest *dB/dt* values at the measurement plane. The average normalized percentage differences between experimental and simulated values on the measured plane were 6.6%, 10.2%, and 5.4% for the *x*-, *y*-, and *z*-elements, respectively. Fig. 3C shows measurements done along the *x*-axis for both the recorded values (solid lines) and the simulated data (dashed lines). For the data acquired along the *x*-axis (indicated by the red line in Fig. 3A) the average normalized percentage differences between the experimental data and the simulated data were 7.3%, 10.9%, and 7.1% for the *x*-, *y*-, and *z*-elements, respectively. The average normalized percentage difference between the measured and simulated data were very consistent for both measurements (2D grid and 1D line). The results confirm quantitatively that the 3-axis coil is operating as intended.

3.3. E-field strength and spatial profiles for the three elements

To assess the stimulation intensity and focality of the 3-axis TMS coil, we calculated the induced E-field on a sphere for the *x*-, *y*-, *x/y*-, and *z*-elements with 75% MSO intensity at 2 cm depth as shown in Fig. 4B. The corresponding *dI/dt* values along with the maximum E-field intensities in Fig. 4B shows that the strength of the *x*-element (45 V/m) is about 50% of the *z*-element (87 V/m) as expected by the winding geometry. The *y*-element elicits a slightly weaker E-field due to its slightly elevated position relative to the *x*-element, however, the vector combination of the *x*- and *y*-elements allows for a stronger E-field under the coil assembly at the 45° orientation. The longitudinal and transverse focality values are defined as the principal axis dimensions of the ellipse-shaped E-field region with amplitude higher than 75% of the maximum (Fig. 4C). The *x*- and *y*-elements as well as the

combination (*x/y)* produce focal stimulation patterns similar to figure-of-eight coils as discussed next.

The most straightforward and efficient way to produce a focal E-field is using two *z*-elements with current pulses of opposite polarity, similar to figure-of-eight coils such as MagVenture Cool-B35 or C-B60 (MagVenture, Farum, Denmark) (see Fig. 5A for the setup). The computationally estimated E-fields are shown in Fig. 5B. The stimulation intensity and focality metrics for all three cases are summarized in Fig. 5C. The results suggest that two *z*-elements can exceed the stimulation intensity of a larger C-B60 (158 V/m compared to 138 V/m) while being as focal as the small-diameter Cool-B35.

3.4. Air cooling performance

The cooling performance results are summarized in Fig. 6. The *z*-element reached the highest temperature. Specifically, without cooling, the temperature rise of the *z*-element was 1.12 times larger than that of the *x*-element and 1.55 times larger than that of the *y*-element. With air cooling, the relative decrease in the maximal temperature reached by all elements was very similar (~ 2 °C). The *y*-element reached its maximum temperature first while the z-element took about 1 min to reach the peak temperature. The rise time is reduced in all three elements in a similar way when the air-cooling method is applied. From the curves it is clear that the *x/y*-elements are thermally more tightly coupled to each other (the temperatures of the elements converge to an identical value after ~ 2 min) as well as the fact that by construction the cooling generally works more efficiently for the *x/y*-unit than for the *z*-element.

Cross-heating data between coils (when a coil is discharged the heat conducts to the other coils) were not further analyzed but the effect is visible in Fig. 6B. Based on the symmetry of the design, the z-element is heated maximal about 4 °C when the *x/y*-element are fired, following a similar curve. When using the air-cooling method, the cross-heating between the *x/y*-assembly and the *z*-element becomes minimal.

In general, when using air cooling all elements started to decrease their temperatures no later than 1 min after the stimulation train ended and especially the *x/y*-elements return to baseline much faster than if no cooling was used. Moreover, cooling the coil from the ambient room temperature of 21° C to ~ 12° C allowed more pulses to be delivered. Thus, air cooling extends the usability of the 3-axis coil for rTMS.

3.5. Estimating the coupling between the 3-axis coil elements and between z-elements of different units in the array configuration

The inductance of the *x*-, *y*-, and *z*-elements were measured as L_x = 11.4 μH, L_y = 12.22 μH, and L_z = 12.64 μH. The inductance of the *z*-element built to measure coupling in the array configuration was $L_{z'}$ = 12.93 μH. The mutual coupling between the *x*-, *y*-, and *z*-elements were calculated as M_{xy} = 0.07 μH, M_{xz} = 0.08 μH, and M_{yz} = 0.045 μH, which gives coupling factors of 0.59%, 0.6%, and 0.36%, respectively. The resistance values measured for the coil elements were R_x = 22 mΩ, R_y = 23 mΩ and R_z = 22 mΩ. The coupling factors between the *z*-elements in the array configuration are shown in Fig. S1. The maximal coupling of 1.8% was found between the pairs in positions 1/2 and 14/15. For the

computational estimation of the mutual inductances between all *x/y/z*-elements in the array configuration, we note that the highest coupling occurs between the *z*-elements in the array as expected (not shown). The calculated coupling factors between all *z*-elements in the array configuration are illustrated in Fig. S2. In this case the maximal coupling obtained was 3.4% between the pairs 12–13. While the pair 12–13 shows highest coupling, the corresponding pair on the left hemisphere, 6–7 shows a slightly lower coupling of 2.66%. However, for other corresponding pairs like 3–7 and 13–16 we obtained very similar values. Given the fact that the measured and simulated coil positions in the array were similar but not exactly identical, the spatial distribution of the coupling between the *z*-element pairs for the measured and the calculated values show a consistent pattern.

We subsequently quantified the coil coupling using the field data when the coils were pulsed either pairwise simultaneously or separately. Fig. 7 shows the results obtained when the *x*- and *y*-elements were activated independently *vs.* combined. The plane plot shows the magnitude of the *dB/dt* and the arrows show the direction of the magnetic field change rate vector. The figure demonstrates that the superposition principle holds as expected: There is a robust agreement between the data acquired when the coils were activated simultaneously and when the data were synthesized as the summation of each element's field obtained separately. From the acquired data, we also calculated the percentage average of the difference between both cases and found the quantities ρ_{xy}, ρ_{xz}, and ρ_{yz} to be 1.9%, 1.2%, and 1.1%, respectively. For all three pair-wise combinations, we observed that the linear superposition principle was valid and therefore the coupling between elements was negligible.

3.6. Example of spatiotemporal field control: the "stepwise field rotation" protocol

As an example of the robust spatiotemporal field control achieved with the 2-channel programmable stimulator prototype and the 3-axis coil, a protocol for "stepwise field rotation" was generated. The protocol consisted of 20 pulses delivered over 2 s to the *x*- and *y*-elements, changing the intensities of each element every 100 ms in order to rotate the produced magnetic field by 18° for each pulse (total rotation of 360°). The target B-field directions are shown on the top of Fig. 8A. Even though we only tested this protocol on the XY plane (due to the 2-channel limitation), the protocol can be generalized for a 3-channel stimulator to orient the magnetic field vector in three dimensions. The protocol was validated by acquiring the produced *dB/dt* pulses on the origin of the grid shown in Fig. 3A using the MagProbe 3D.

The results from the stepwise field rotation experiment are summarized in Fig. 8. The first three entries of the protocol are shown in Fig. 8A. Channel 1 and Channel 2 were connected to the *x*- and *y*-elements of the 3-axis coil, respectively. The third column of the protocol indicates the delay between pulses in microseconds. The acquired *dB/dt* data are plotted as a function of time to show the synchronization of the delivered pulses to the *x*- and *y*-elements (Fig. 8B). A zoom-in view of one of these pulses is shown at the bottom of Fig. 8C, where the changes in the induced voltages at the probe are related to the produced x and y components of the *dB/dt* vector (the *z* component is almost zero for this particular protocol). The maximal values of *dB/dt* at the beginning of each pulse during the protocol were

selected to Fig. 8C to illustrate the measurements as vectors in a polar plot. Each vector corresponds to a pulse, starting with the vector numbered 1 (only cartesian *x* component produced by *y*-element fired alone at 50% MSO) and then going counterclockwise as the pulses were given. The results show that the measured *dB/dt* vectors recapitulate the intended pulse sequence highly accurately.

To illustrate how the rotating field protocol could be used to stimulate the brain with different E-field orientation for each step, Fig. S3 shows the computational modeling results using an anatomically realistic head model. A similar rotation pattern is also produced for the induced E-field. In Fig. S3, the selected directions were shown and numbered according to the polar representation of Fig. 8C with the angle defined with respect to the *x*-element.

3.7. Computational multichannel targeting using a 3-axis coil array

A multichannel TMS array was simulated with 16 3-axis coils positioned around the head surface to cover both cortical hemispheres with the array geometry as shown in Fig. 9A. The linear combination of the induced E-fields of the forty-eight coil units to synthesize the desired stimulation target pattern and orientation was found by optimization using a minimum norm estimate (MNE) based approach (Ruohonen and Ilmoniemi, 1998). For MNE optimization, the *dI/dt* was constrained to 50 A/ μs that is a rather conservative value < 50% of MSO (see, Fig. 2). The constrained optimization run time varies from 1 s to 250 s depending on the resolution of the cortical surface mesh used to sample the E-fields for the target field approach. Due to the overdetermined nature of the problem, the size of the system matrix can be reduced by more than 10 times without significant changes in the results. As the computational time is not critical for the present study, we employed the full high-resolution mesh.

The multichannel 3-axis coil array was able to shift the E-field focal point as the target field and angle changes across the motor cortex as illustrated in Fig. 9B. For all targets shown in Fig. 9B, we were able to reach a maximum E-field of 100 V/m at the gray/white matter boundary at *dI/dt* values below 50 A/ μs (Fig. 9C). For practical applications it would be possible to further optimize the multichannel TMS array configuration to increase the stimulation intensity and focality while reducing the required stimulator output intensity.

4. Discussion

Here, we designed, built, and validated a 3-axis coil that is intended to be used as the basic unit in multichannel TMS arrays. The key motivation behind our 3-axis coil is that it *i*) provides simple and effective geometric decoupling between the elements, *ii*) offers a compact footprint that can be used to increase the degrees of freedom (number of elements) available for the computational algorithms used for electronic targeting, *iii*) allows fully modular system development with any desired number of array units, *iv*) permits conformal positioning of each individual coil unit tangential to scalp surface for variable head sizes, and *iv*) enables efficient and safe stimulation even with a simple air cooling mechanism.

The 3-axis multichannel TMS array system is a mixture of ‘traditional’ TMS arrays where the *z*-elements corresponds to the basic array elements that are augmented with two

additional channels, the *x* and *y*-elements. A somewhat similar construction to the *x*- and *y*-elements has been previously proposed to generate a continuously rotating E-field (Rotem et al., 2014). However, our design is significantly different in that the *x*- and *y*-elements are wound in an interlaced fashion and integrated with the *z*-element to maximize efficiency and in its intended use as the basic unit of a human multichannel TMS array to increase the targeting efficiency and accuracy near the TMS unit center. As illustrated by our results, the *x*-element's efficiency is only ~50% of the efficiency of the *z*-element, but when combined with the *y*-element as well as neighboring 3-axis units, they act as critical elements to add to the flexibility and efficiency of targeting. Our goal was to construct a simple 3-axis coil geometry such that the inductances of all *x*-, *y*-, and *z*-elements are matched resulting in identical pulse widths, enabling the use of the coil with traditional bi-phasic stimulators. In the future, efficiency of the *x*- and *y*-elements may be further increased by relaxing the constraint of matched inductances and adhering to more advanced TMS coil design methods (Koponen et al., 2015).

Despite the reduced efficiency in the *x*- and *y*-elements, the critical benefit of our design is that the elements become automatically decoupled. Indeed, the results show that the mutual inductances between the 3-axis elements are less than ~0.1 μH, which is about 1% of the typical self-inductance of ~10 μH. The results obtained for the coupling between the *z*-elements of different units in the array configuration show us that the coupling in the worst case will be between 2 and 3%. Even though we have not measured the coupling between *x*-elements or *x/y*-elements of different units in the array configuration, the computational results indicate that they do not exceed the values obtained for the *z*-elements of different units. Furthermore, the coupling between the *x*- and *y*-elements of two neighboring 3-axis coils can be minimized by rotating the 3-axis TMS coils with respect to their own z axis so that the *x*- and *y*-elements are as close to 45° relative to each other as possible, which is expected to render the mutual inductance between elements of different units (interunit coupling) to be in the range of 1 to 2% across the entire array. While relatively straightforward methods to compensate for the coil coupling have been presented (Han et al., 2004), the geometrically decoupled array offers a highly robust and simple approach to mitigate this issue.

Since the coils are wound using a relatively small diameter wire to enable efficient stimulation with a small diameter 3-axis coil, heating was worse than for commercial coils as confirmed by our experiments with heating per pulse ~0.7 °C/pulse at 75% MSO. To reduce the coil heating, some type of active cooling is needed. The air-cooling approach was chosen for the current design to simplify the construction, as a watertight chassis is somewhat more challenging and costly to fabricate. Assuming 3 scfm air is needed per each coil unit, a 16-unit 3-axis system would require less than 50 scfm air flow, which is in the range of a standard off-shelf medium-sized compressor. The use of room temperature air for the cooling is also possible, however we decided to use cooled air to allow additional pulses before reaching the safety limit of 41 °C. As our results show, the simple air cooling enables extended single-pulse and paired-pulse experiments as well as delivering a couple of 1–2 second trains of rTMS with a few minutes of cooling afterwards. However, if more aggressive protocols are desired, liquid cooling systems can be readily developed. The coil heating for a commercially available non-cooled small diameter TMS coil, the MagVenture

MC-B35 was assessed using the same protocol as described in the methods (75% intensity, 20 pulses in 1 second, following 6 min observation). The heating per pulse was ~0.4 °C/pulse, and the temperature remained 4 °C above the baseline after 6 min. These results are in the same range as the values for the *x/y*-elements (see, Fig. 6) but somewhat lower than the *z*-element. However, taking into account that the E-field intensity produced by the MagVenture Cool-B35 coil with 75% MSO is significantly smaller than the field produced by our two *z*-elements together (see, Fig. 5), we can conclude that the basic non-cooled performance of our *z*-elements is comparable to commercially available coils of similar physical dimensions when run in the equivalent 'figure-of-eight' mode using two independent stimulators.

The electromagnetic simulation results using a simplified spherical model show that a juxtaposition of two *z*-elements in a figure-of-eight configuration gives an E-field amplitude (stimulation intensity) comparable to the 'industry standard' MagVenture C-B60 and spatial E-field dispersion (focality) that is comparable to 'most compact available' Cool-B35 coil. The key to achieving this 'double win' is naturally that the two *z*-elements are driven by independent stimulator units delivering double the energy. The results provided strong evidence that an array of 3-axis coils will be capable of suprathreshold stimulation. This was further confirmed in our simulations with an anatomically realistic head model and a sixteen 3-axis TMS coil array covering the whole head. Even with the intensity of each channel limited to < 50% of MSO, the E-field intensity of ~ 100 V/m was readily produced at several targets across the motor cortex. Taken together, the results indicate that the envisioned modular 3-axis multichannel TMS array system will offer a comfortable headroom for suprathreshold stimulation experiments across individuals with variable motor thresholds.

A key enabling technology for the multichannel TMS array concept is the high-resolution modeling of the intracranial E-fields as the stimulation of different targets are achieved by adjusting the currents in the coil unit's elements based on the computationally predicted values. To this end, several approaches such as the finite element method (FEM) (Windhoff et al., 2013) and BEM-FMM based methods (Htet et al., 2019; Makarov et al., 2020, 2018) are available. To maximize the potential of the computational targeting approach, the MRI acquisition and head model segmentation techniques need also to be optimized. The importance of the patient-specific E-field modeling in this domain is evident and further systematic computational studies on how the E-field can be steered across different multichannel array designs and individual patients are necessary to quantify the expected system performance. Another aspect of our efforts is to generalize the 3-axis TMS coil technology to become usable inside the MRI environment (Navarro de Lara et al., 2020). The MR-compatible 3-axis TMS coils however require certain modifications to improve the structural stability in order to withstand the external forces and torques due to the 3T MRI main magnetic field. The combination of stimulation and neuroimaging (Siebner et al., 2009) is particularly powerful for elucidating the causal relationships between different nodes of cortical networks. The capability to perform concur-rent fMRI and multifocal TMS would drastically expand the scope of potential applications in such experiments.

5. Conclusion

We designed, built, and validated a 3-axis TMS coil by comparing computational modeling results with empirical field mapping data. We used a custom-made two-channel programmable TMS stimulator to demonstrate that spatiotemporal control of multiple coils can be performed accurately. The computational E-field simulations show that an array consisting of such 3-axis coils can be utilized to electronically shift the position of the E-field focal spot with stimulation intensity comparable to commercial TMS coils. The proposed air-cooled 3-axis coil meets the technical requirements for general-purpose multichannel TMS array systems justifying further development and first-in-human studies.

Supplementary Material

Refer to Web version on PubMed Central for supplementary material.

Acknowledgments

We want to thank Henrik Corfitzen, Jesper Bruus-Jensen and Yordan Todorov (MagVenture, Farum, Denmark) for providing information about dimensions of the TMS coils (H.C. and Y.T.) as well as continuing support during the tests with the custom-built 2-channel stimulator (H.C. and J.B.-J.). We also thank Tori Turpin (MGH Martinos Center) for helpful comments on the manuscript. Research supported by NIH R00EB015445, R01MH111829 and the Ralph and Mariam Falk Medical Research Trust.

Declaration of Competing Interest

L.N.L. is a named inventor in a TMS-related patent (US9924889). A.M., K.P. and D.P. are employed by Tristan Technologies, Inc., San Diego, that is a for-profit company with commercial interests in TMS device development. Y.O. is the owner of Moment Technologies, LLC, Boston, MA, that is a for-profit company with commercial interest in TMS device development. Both Tristan Technologies and Moment Technologies are recipients of subawards from the NIH-funded grant R01MH111829 supporting this work. S.N.M is partially employed by NEVA (Bio)electromagnetics, LLC, Yarmouth Port, MA, that is a for-profit company with commercial interest in electromagnetic human modeling and neuromodulation device development. A.N. and T.R. are named inventors in TMS-related patent applications. M.D. declares no competing interests.

References

Barker AT, Jalinous R, Freeston IL, 1985 Non-invasive magnetic stimulation of the human cortex. Lancet 1, 1106–1107. [PubMed: 2860322]

Ferbert A, Priori A, Rothwell JC, Day BL, Colebatch J, Marsden CD, 1992 Inter-hemispheric inhibition of the human motor cortex. J. Physiol. 525–546.

Goetz SM, Kozyrkov IC, Luber B, Lisanby SH, Murphy DLK, Grill WM, Peterchev AV, 2019 Accuracy of robotic coil positioning during transcranial magnetic stimulation. J. Neural Eng. 16. doi: 10.1088/1741-2552/ab2953.

Groppa S, Werner-Petroll N, Münchau A, Deuschl G, Ruschworth MFS, Siebner HR, 2012 A novel dual-site transcranial magnetic stimulation paradigm to probe fast facilitatory inputs from ipsilateral dorsal premotor cortex to primary motor cortex. Neuroimage 62, 500–509. doi: 10.1016/j.neuroimage.2012.05.023. [PubMed: 22626848]

Han BH, Chun IK, Lee SC, Lee SY, 2004 Multichannel magnetic stimulation system design considering mutual couplings among the stimulation coils. IEEE Trans. Biomed. Eng. 51, 812–817. doi: 10.1109/TBME.2004.824123. [PubMed: 15132507]

Htet AT, Burnham EH, Noetscher GM, Pham DN, Nummenmaa A, Makarov SN, 2019a Collection of CAD human head models for electromagnetic simulations and their applications. Biomed. Phys. Eng. Express 5. doi: 10.1088/2057-1976/ab4c76.

Koponen LM, Nieminen JO, Ilmoniemi RJ, 2018 Multi-locus transcranial magnetic stimulation — Theory and implementation. Brain Stimul. 11, 849–855. doi: 10.1016/j.brs.2018.03.014. [PubMed: 29627272]

Htet AT, Saturnino GB, Burnham EH, 2019b Comparative Performance of the Finite Element Method and the Boundary Element Fast Multipole Method for Problems Mimicking Transcranial Magnetic Stimulation (TMS). Journal of Neural Engineering 16 (2).

Koponen LM, Nieminen JO, Ilmoniemi RJ, 2015 Minimum-energy coils for transcranial magnetic stimulation: application to focal stimulation. Brain Stimul. 8, 124–134. doi: 10.1016/j.brs.2014.10.002. [PubMed: 25458713]

Lancaster JL, Narayana S, Wenzel D, Luckemeyer J, Roby J, Fox P, 2004 Evaluation of an image-guided, robotically positioned transcranial magnetic stimulation system. Hum. Brain Mapp. 22, 329–340. doi: 10.1002/hbm.20041. [PubMed: 15202111]

Makarov SN, Noetscher GM, Raij T, Nummenmaa A, 2018 A quasi-static boundary element approach with fast multipole acceleration for high-resolution bioelectromagnetic models. IEEE Trans. Biomed. Eng. 65, 2675–2683. doi: 10.1109/TBME.2018.2813261. [PubMed: 29993385]

Makarov SN, Wartman WA, Daneshzand M, Fujimoto K, Raij T, Nummenmaa A, 2020 A software toolkit for TMS electric-field modeling with boundary element fast multipole method: an efficient MATLAB implementation. J. Neural Eng. doi: 10.1088/1741-2552/ab85b3.

Navarro de Lara LI, Golestanirad L, Makarov SN, Stockmann JP, Wald LL, Nummenmaa A, 2020 Evaluation of RF interactions between a 3T birdcage transmit coil and transcranial magnetic stimulation coils using a realistically shaped head phantom. Magn. Reson. Med. 84, 1061–1075. doi: 10.1002/mrm.28162. [PubMed: 31971632]

Rotem A, Neef A, Neef NE, Agudelo-Toro A, Rakhmilevitch D, Paulus W, Moses E, 2014 Solving the orientation specific constraints in transcranial magnetic stimulation by rotating fields. PLoS One 9. doi: 10.1371/journal.pone.0086794.

Roth Y, Levkovitz Y, Pell GS, Ankry M, Zangen A, 2014 Safety and characterization of a novel multi-channel TMS stimulator. Brain Stimul. 7, 194–205. doi: 10.1016/j.brs.2013.09.004. [PubMed: 24529836]

Ruohonen J, Ilmoniemi RJ, 1998 Focusing and targeting of magnetic brain stimulation using multiple coils. Med. Biol. Eng. Comput. 36, 297–301. doi: 10.1007/BF02522474. [PubMed: 9747568]

Ruohonen J, Karhu J, 2010 Navigated transcranial magnetic stimulation. Neurophysiol. Clin. 40, 7–17. doi: 10.1016/j.neucli.2010.01.006. [PubMed: 20230931]

Siebner H, Bergmann T, Bestmann S, Massimini M, Johansen-Berg H, Mochizuki H, Bohning D, Boorman E, Groppa S, Miniussi C, Pascual-Leone A, Huber R, Taylor P, Ilmoniemi R, De Gennaro L, Strafella A, Kahkonen S, Kloppel S, Frisoni G, George M, Hallet M, Brandt S, Rushworth M, Ziemann U, JC R, Ward N, Cohen L, Baudewig J, Paus T, Y U, Rossini P., 2009 Consensus paper: combining transcranial stimulation with neuroimaging. Brain Stimul. 2, 58–80. [PubMed: 20633405]

Van Essen DC, Ugurbil K, Auerbach E, Barch D, Behrens TEJ, Bucholz R, Chang A, Chen L, Corbetta M, Curtiss SW, Della Penna S, Feinberg D, Glasser MF, Harel N, Heath AC, Larson-Prior L, Marcus D, Michalareas G, Moeller S, Oostenveld R, Petersen SE, Prior F, Schlaggar BL, Smith SM, Snyder AZ, Xu J, Yacoub E, 2012 The human connectome project: a data acquisition perspective. Neuroimage 62, 2222–2231. doi: 10.1016/j.neuroimage.2012.02.018. [PubMed: 22366334]

Windhoff M, Opitz A, Thielscher A, 2013 Electric field calculations in brain stimulation based on finite elements: an optimized processing pipeline for the generation and usage of accurate individual head models. Hum. Brain Mapp. 34, 923–935. doi: 10.1002/hbm.21479. [PubMed: 22109746]

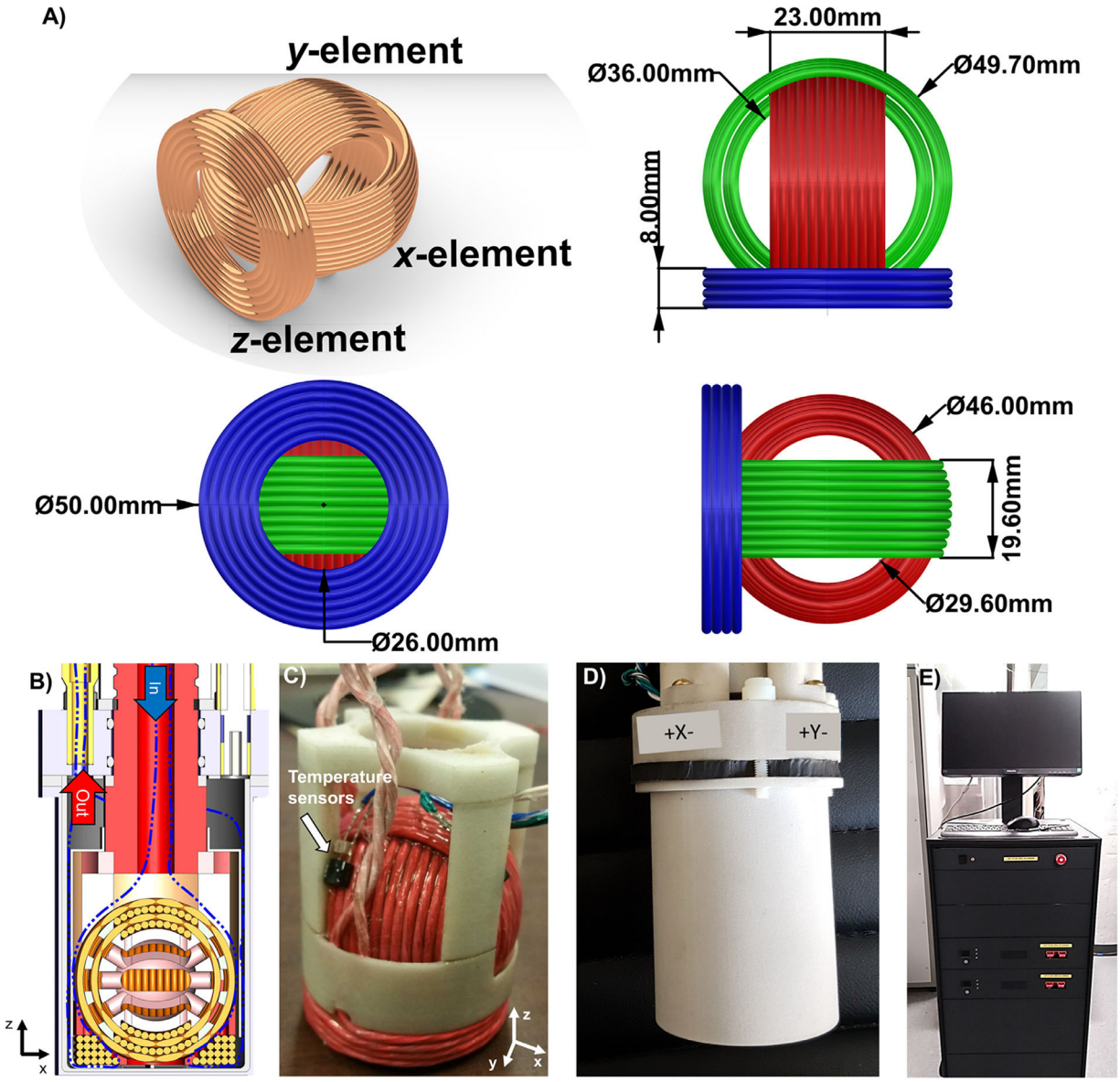

Fig. 1. 3D-CAD model/design of the 3-axis TMS coil prototype and two-channel programmable stimulator prototype.

A) The 3-axis coil consists of three perpendicular solenoid coils the *x*-element (green), *y*-element (red) and *z*-element (blue). The *x*/*y*-elements are wound in an interlaced fashion into each other and embedded to the z-element. Dimensions are annotated in the figure. **B)** Schematic of the final design of the 3-axis coil, including the air-cooling system. Cool air (thick blue arrow) is injected through the center of the coil while the warm air (red arrow) exits through the side outlets. Connectors to each coil are placed directly on top of the coil. **C)** Photograph of the of the inner part of the fabricated coil including positions of the temperature sensors. **D)** Photograph of the final 3-axis coil prototype including plastic chassis. **E)** Photograph of the 2-channel programmable TMS stimulator system custom-built by MagVenture (Farum, Denmark).

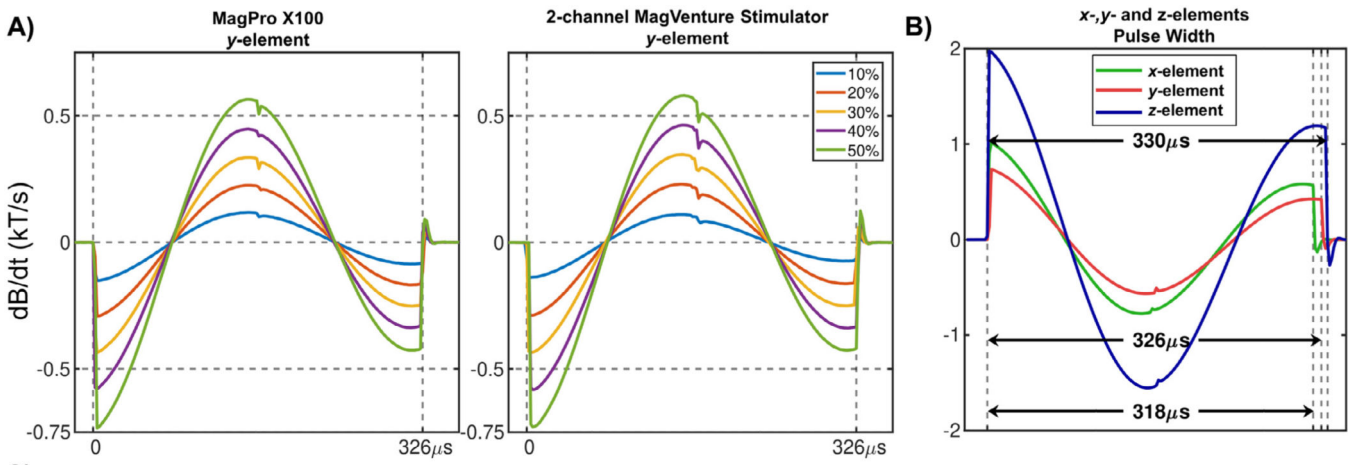

C)

Stimulator Output	*x*-element (*dI/dt* A/μs, dB/dt kT/s)	*y*-element (*dI/dt* A/μs, dB/dt kT/s)	*z*-element (*dI/dt* A/μs, dB/dt kT/s)
10%	10.5 / 0.1968	10.5 / 0.1439	10.5 / 0.7574
20%	25 / 0.4	24 / 0.2924	23.5 / 1.5648
30%	38 / 0.5971	37 / 0.4334	35 / 2.3317
40%	53 / 0.8042	49 / 0.5816	49 / 3.1367
50%	67 / 1.0143	63 / 0.7325	61.5 / 3.9598

Fig. 2. Magnetic pulse measurements of the 3-axis coil.

A) Measured *dB/dt* time courses of the MagPro X100 (left panel) *vs.* the 2-channel programmable stimulator prototype for *y*-element (right panel). Only the cartesian *x* component is shown as the *y* and *z* components are negligible. **B)** Measured *dB/dt* data for all three elements of the 3-axis TMS coil: only the relevant cartesian *x/y/z* component for each element is shown. The figure shows the pulse widths obtained for each element. The pulse obtained with the *z*-element was scaled by a factor of 1/2 for display purposes. **C)** Values obtained from the calibration data (maximal current rates-of-change *dI/dt*) and corresponding magnetic field rate (*dB/dt*) values for the stimulator output intensities from 10% to 50% for each element of the 3-axis coil.

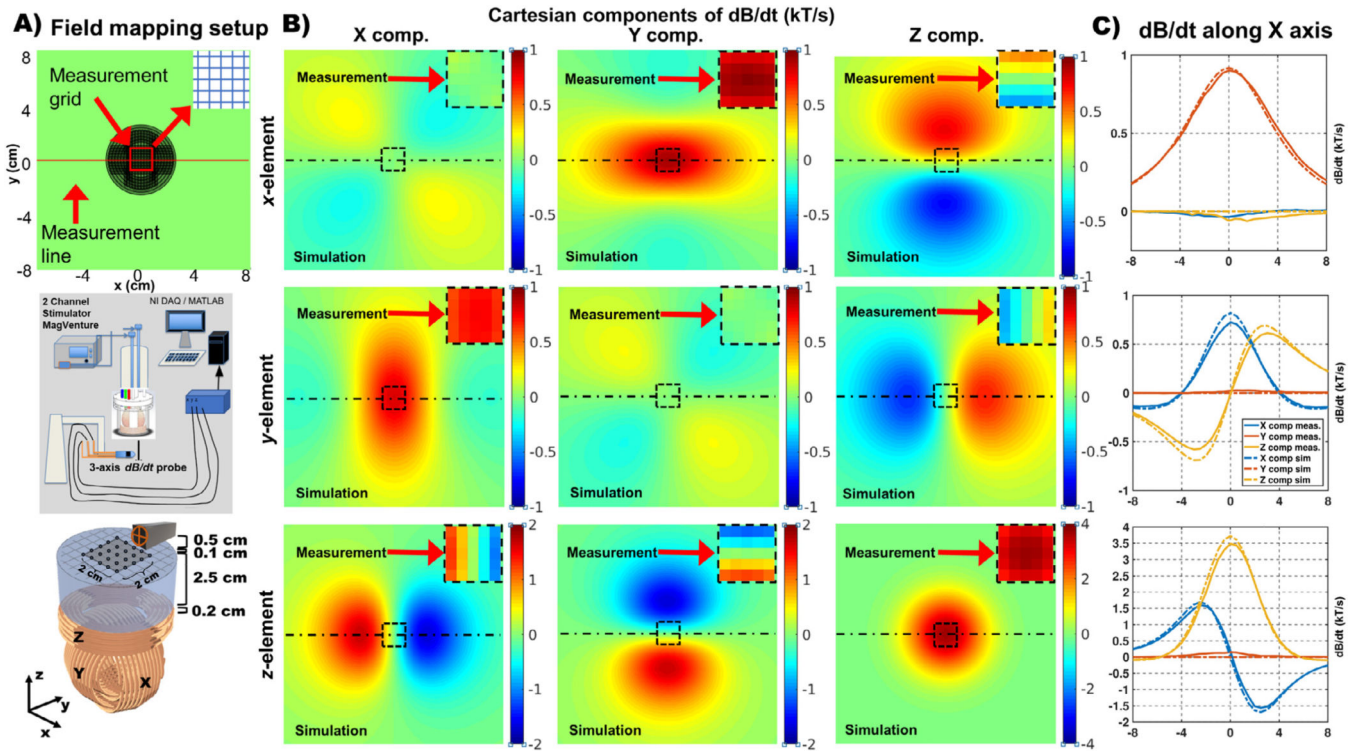

Fig. 3. Magnetic field mapping of the 3-axis coil.

A) Field mapping setup used for the measurements. Using the MagProbe 3D, the magnetic field rate-of-change 2D spatial maps were acquired 3.3 cm away from the coil on a 4 cm ^{2} plane covering from −1 cm to 1 cm in both *x* and *y* directions in 0.5 cm steps and following a 5 × 5 grid. The 1D measurement line refers to the x-axis (indicated by the red line) and data was collected with 0.5 cm steps from $x = -8$ cm to $x = +8$ cm. **B)** Electromagnetic simulation *vs.* measurement results of the magnetic field rate-of-change for each cartesian component for the *x*-, *y*-, and *z*-elements. The simulation range was extended to increase the field of view of the topographies. **C)** Measured magnetic field rate-of-change over the central line of the 3-axis coil. All three cartesian components are shown in the plot.

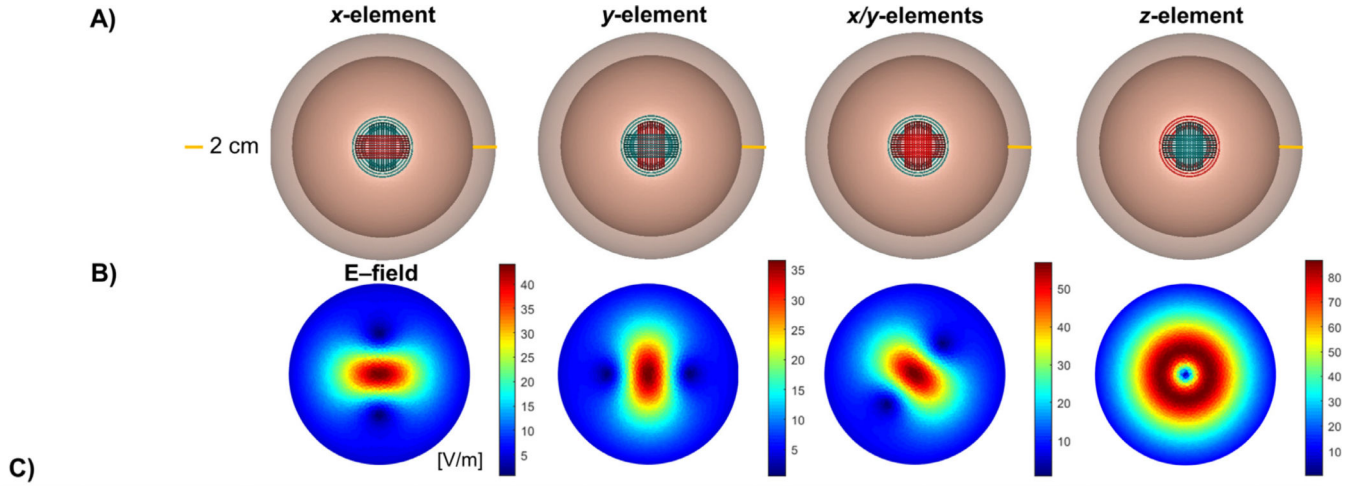

Element	*x*-element	*y*-element	*x*/*y*-element	*z*-element
75% Intensity, $\frac{dI}{dt}$ $(A/\mu s)$	102.5	96.7	99	94
Maximum E (V/m)	45	37	57	87
Longitudinal Focality metric (cm)	4.4	4.6	4.3	N/A
Transverse Focality metric (cm)	2.4	2.5	2.4	N/A

Fig. 4. Simulation of the induced E-field profiles of the 3-axis coil elements using a sphere model. **A)** Simulation setup. The inner and outer sphere radii are 10 and 12 cm, respectively. The coils are placed such that the z-element is tangential to the sphere, and the activated elements are shown in red. **B)** The bottom row shows the corresponding induced E-field amplitude profile for each element on the surface of the inner sphere, approximately at 2 cm depth from the coil. **C)** Summary of the stimulation intensity and focality metrics of the 3-axis coil elements on the sphere. The *dI/dt* values correspond to 75% of the MSO.

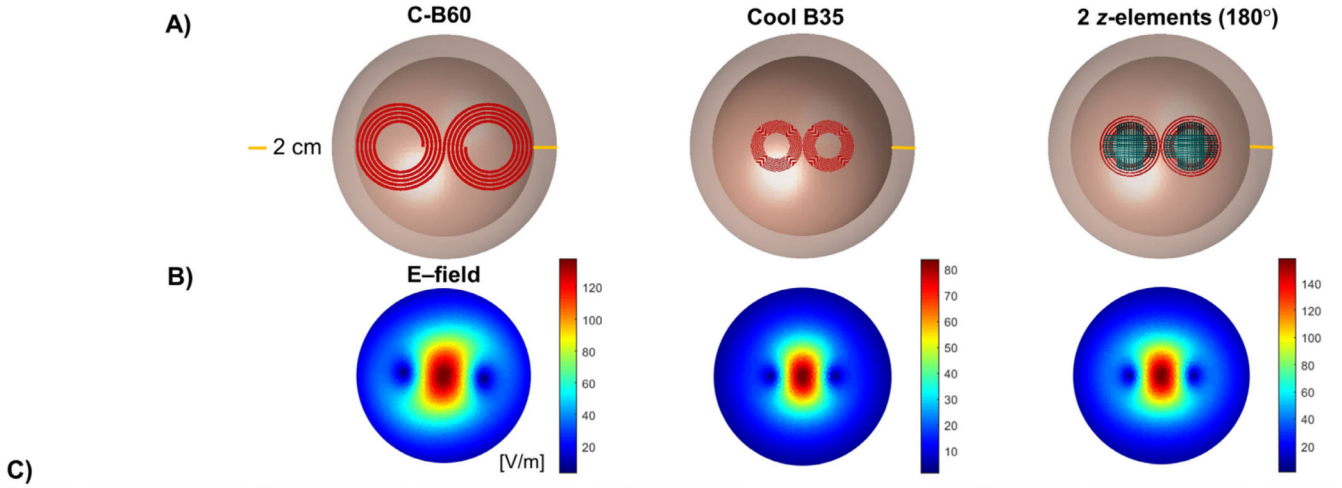

C)

Coil Type	C-B60	Cool B35	2 z-elements
75% Intensity, $\frac{dI}{dt}$ $(A/\mu s)$	116	101	94
Maximum E (V/m)	**138**	**89**	**158**
Longitudinal Focality (cm)	4.7	3.6	3.7
Transverse Focality (cm)	3	2.3	2.4

Fig. 5. Comparison of the induced E-field from two combined *z*-elements of two 3-axis coils with approximate models of commercial TMS coils.

A) The simulated coil models including two commercial coils (C-B60 and Cool-B35) and a pair of *z*-elements combined in a figure-of-eight configuration. **B)** E-field intensities calculated using a spherical model displayed at 2 cm distance under the coils. **C)** The stimulation intensity and focality metrics for the different coil models. The *dI/dt* values are reported at 75% intensity of the stimulator maximum.

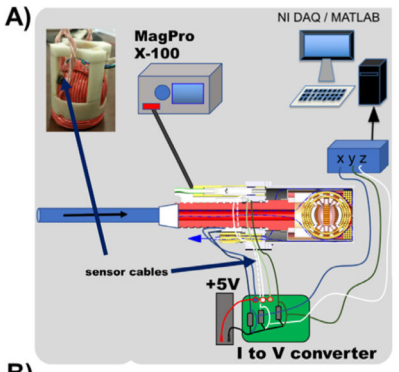

C)

	Cooling	$T_{baseline}$	T_{max}	Δ°C	Δ°C / pulse	$T_{1/2}$	R^2
x-elem.	No air	20.1	32.6	12.5	0.63	275.2 s	0.8447
	Air cooling 3 sfcm	11.8	21.5	9.7	0.49	56.4 s	0.9528
y-elem.	No air	20.4	29.4	9	0.45	541.1 s	0.9253
	Air cooling 3 sfcm	12	19.2	7.2	0.36	102.9 s	0.931
z-elem.	No air	20.8	34.8	14	0.7	232.8 s	0.9969
	Air cooling 3 sfcm	11.4	23.2	11.8	0.59	143.9 s	0.998

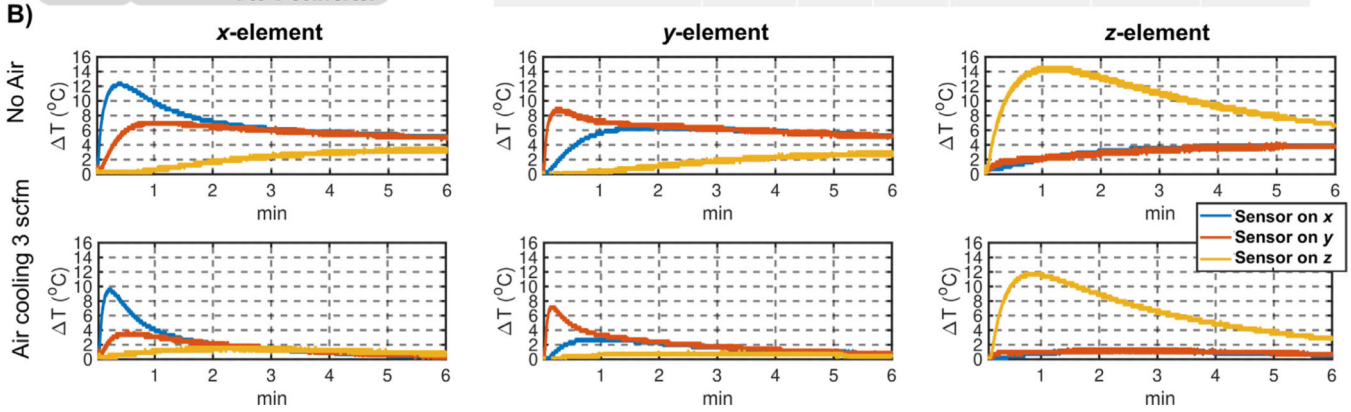

Fig. 6. Coil heating/cooling measurements.

A) Setup used to monitor the temperature of the three elements when the MagPro X100 stimulator was used to discharge one train of 20 pulses per second at 75% MSO. **B)** Temperature time courses when each element was separately activated. The first row of figures shows the results when no air cooling was used, and the second row when cooled air between 12° ~ 15 °C was injected with a flow rate of 3 scfm. **C)** Performance values for the *x*-, *y*-, and *z*-elements extracted from the temperature time courses.

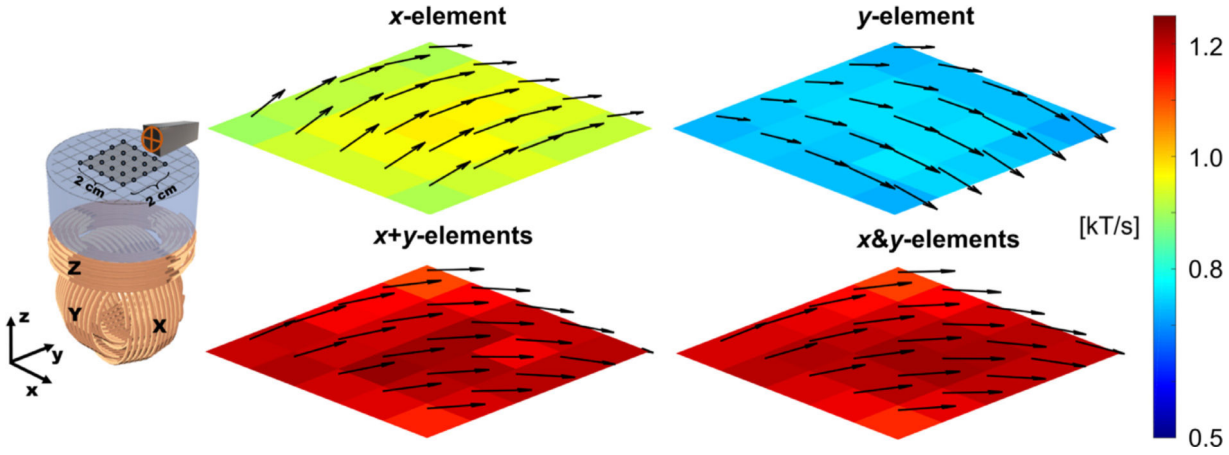

Fig. 7. Testing the coil coupling through the principle of linear superposition.

Top) Magnetic field rate-of change visualization with both magnitude (color-coded image data) and orientation (black arrows) for each acquired point on the grid for *x*-element (left panel) and *y*-element (right panel) when activated separately. **Bottom)** Magnetic field rate-of change visualization when the results of the individual coils where algebraically summed (*x* + *y*-elements panel) *vs.* when the coils were activated simultaneously (*x* & *y*-elements panel).

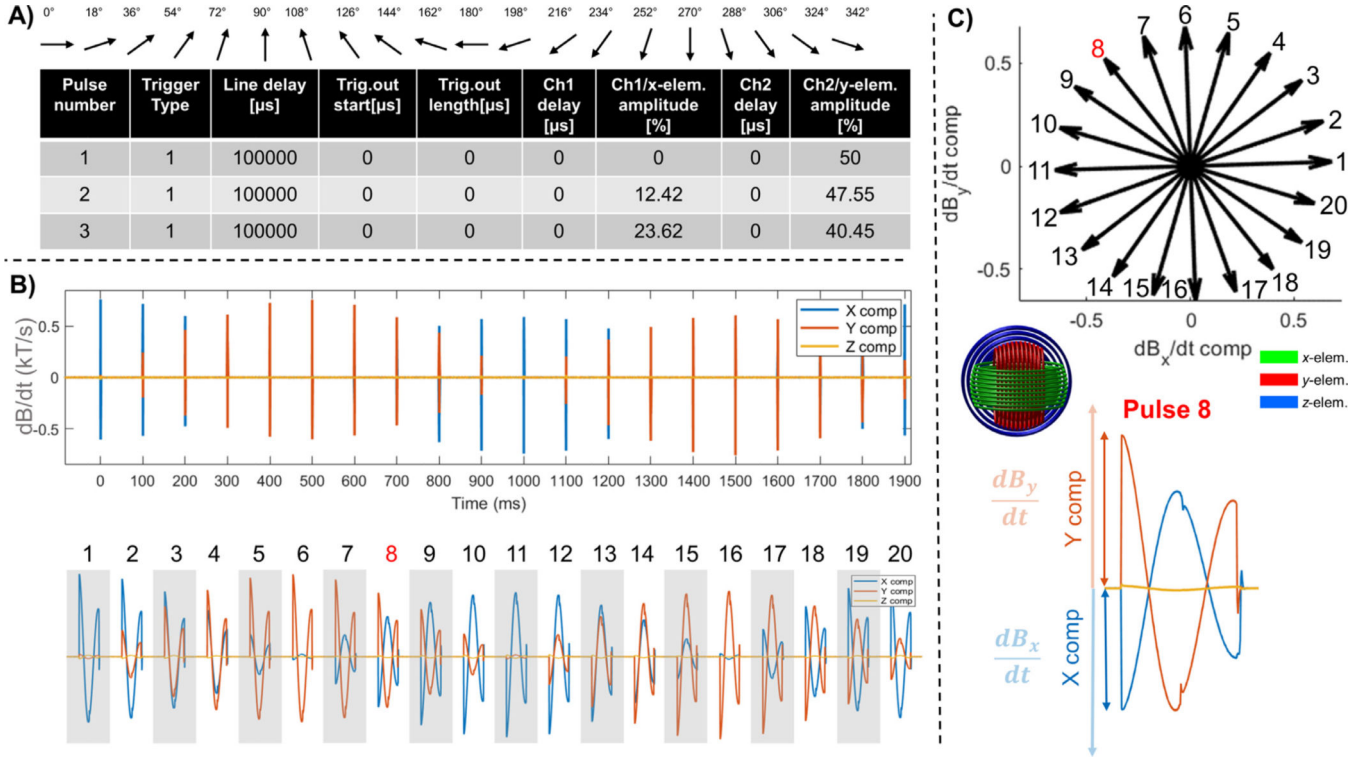

Pulse number	Trigger Type	Line delay [μs]	Trig.out start[μs]	Trig.out length[μs]	Ch1 delay [μs]	Ch1/x-elem. amplitude [%]	Ch2 delay [μs]	Ch2/y-elem. amplitude [%]
1	1	100000	0	0	0	0	0	50
2	1	100000	0	0	0	12.42	0	47.55
3	1	100000	0	0	0	23.62	0	40.45

Fig. 8. Spatiotemporal field control: the “stepwise field rotation” protocol.

A) Top. The intended magnetic field directions produced by the stepwise field rotation protocol. **Bottom.** First three lines of the protocol that was programmed and executed with the 2-channel system. The third column represents the time between two pulses. Individual delays can be programmed for each channel/element as well as trigger outputs to synchronize the data acquisition. **B) Top.** Acquired signal using the MagProbe 3D during the protocol. **Bottom.** Pulses are zoomed in to depict how the intensities for each component change over time to produce the rotation of the field. **C) Top.** Polar representation of the acquired *dB/dt* vector. The protocol starts in *x* direction (only *y*-element was activated, line 1 of the protocol shown in Fig. 8 A) and rotates counterclockwise. **Bottom.** Zoom-in view of the acquired pulse number 8. The maximal value acquired at the beginning of the pulse is the value used in the polar representation of the measured pulses depicted on the top.

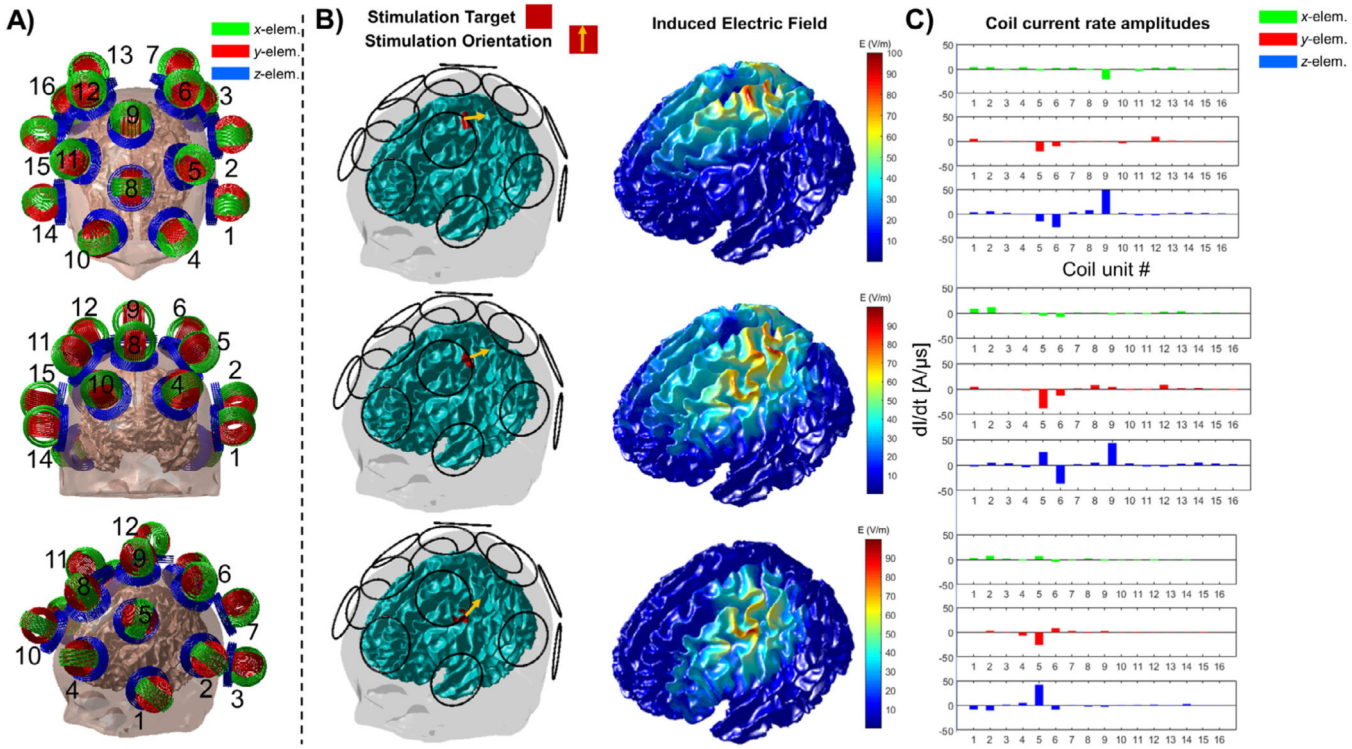

Fig. 9. Simulation of anatomically realistic computational targeting using a multichannel 3-axis TMS coil array.

A) Layout of the 3-axis coil array over the subject's head model (different views). **B)** Stimulation target region of interest areas (red patches) and E-field orientations (yellow vectors). The stimulation targets are selected on the precentral gyrus along the motor area. The multichannel 3-axis coil array can shift the target location and achieve relatively strong and focused induced E-fields around the desired area without coil movement. The induced E-field target amplitude was set to 100 V/m. Black circles show the position on the *z*-element of the 3-axis TMS units over the subject's head. **C)** The coil dI/dt amplitudes obtained from constrained minimum norm optimization with maximum *dI/dt* set to 50 A/µs for each of the individual *x/y/z*-elements.